nature catalysis

Article

https://doi.org/10.1038/s41929-023-00910-x

Ultrasmall amorphous zirconia nanoparticles catalyse polyolefin hydrogenolysis

Received: 18 April 2022

Accepted: 3 January 2023

Published online: 16 February 2023

Check for updates

Shaojiang Chen[1,13], Akalanka Tennakoon[1,2,13], Kyung-Eun You[3,13], Alexander L. Paterson[1], Ryan Yappert[4], Selim Alayoglu[5], Lingzhe Fang[6], Xun Wu[1,2], Tommy Yunpu Zhao[7], Michelle P. Lapak[7], Mukunth Saravanan[1], Ryan A. Hackler[8], Yi-Yu Wang[1,2], Long Qi[1], Massimiliano Delferro[8,9], Tao Li[6,10], Byeongdu Lee[10], Baron Peters[4], Kenneth R. Poeppelmeier[11], Salai C. Ammal[3], Clifford R. Bowers[7,12], Frédéric A. Perras[1], Andreas Heyden[3] ✉, Aaron D. Sadow[1,2] ✉ & Wenyu Huang[1,2] ✉

Carbon–carbon bond cleavage reactions, adapted to deconstruct aliphatic hydrocarbon polymers and recover the intrinsic energy and carbon value in plastic waste, have typically been catalysed by metal nanoparticles or air-sensitive organometallics. Metal oxides that serve as supports for these catalysts are typically considered to be inert. Here we show that Earth-abundant, non-reducible zirconia catalyses the hydrogenolysis of polyolefins with activity rivalling that of precious metal nanoparticles. To harness this unusual reactivity, our catalytic architecture localizes ultrasmall amorphous zirconia nanoparticles between two fused platelets of mesoporous silica. Macromolecules translocate from bulk through radial mesopores to the highly active zirconia particles, where the chains undergo selective hydrogenolytic cleavage into a narrow, C_{18}-centred distribution. Calculations indicated that C–H bond heterolysis across a Zr–O bond of a $Zr(O)_2$ adatom model for unsaturated surface sites gives a zirconium hydrocarbyl, which cleaves a C–C bond via β-alkyl elimination.

Metal oxides are ubiquitous in catalysis as supports for active species or as catalysts themselves. Active oxides, such as those of molybdenum, tungsten or rhenium, can react with unsaturated hydrocarbons in situ to generate surface alkylidene ($M = CR_2$) sites for olefin metathesis[1]. In contrast, the robust metal oxygen bonds of non-reducible oxides are used to create three-dimensional (3D) architectures, such as in zeolites and mesoporous materials. In catalytic reactions, such materials either make use of acidic or basic surface sites or act as supports for reduced metal nanoparticles, single-atom catalysts or surface organometallic chemistry (SOMC) species, rather than forming metal–carbon bonds

[1]US Department of Energy, Ames National Laboratory, Iowa State University, Ames, IA, USA. [2]Department of Chemistry, Iowa State University, Ames, IA, USA. [3]Department of Chemical Engineering, University of South Carolina, Columbia, SC, USA. [4]Department of Chemical and Biomolecular Engineering, University of Illinois at Urbana-Champaign, Urbana, IL, USA. [5]Center for Catalysis and Surface Science, Northwestern University, Evanston, IL, USA. [6]Department of Chemistry and Biochemistry, Northern Illinois University, DeKalb, IL, USA. [7]Department of Chemistry, University of Florida, Gainesville, FL, USA. [8]Chemical Sciences and Engineering Division, Argonne National Laboratory, Lemont, IL, USA. [9]Pritzker School of Molecular Engineering, University of Chicago, Chicago, IL, USA. [10]X-ray Science Division, Argonne National Laboratory, Lemont, IL, USA. [11]Department of Chemistry, Northwestern University, Evanston, IL, USA. [12]National High Magnetic Field Laboratory, University of Florida, Gainesville, FL, USA. [13]These authors contributed equally: Shaojiang Chen, Akalanka Tennakoon, Kyung-Eun You. ✉e-mail: heyden@cec.sc.edu; sadow@iastate.edu; whuang@iastate.edu

https://doi.org/10.1038/s41929-023-00910-x

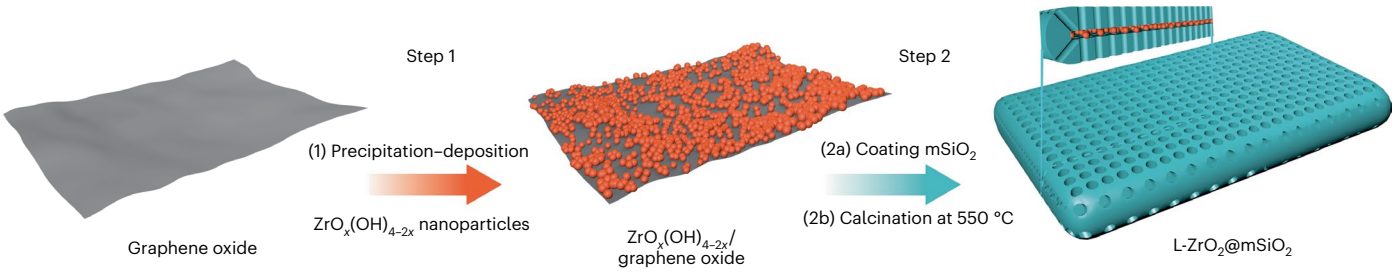

Fig. 1 | Construction of L-ZrO_2@$mSiO_2$. The construction of L-ZrO_2@$mSiO_2$ involves three steps: (1) precipitation–deposition of $ZrO_x(OH)_{4-2x}$ nanoparticles onto graphene oxide, (2a) coating of $mSiO_2$ onto $ZrO_x(OH)_{4-2x}$/graphene oxide and (2b) calcination at 550 °C.

themselves. In principle, in situ conversion of non-reducible metal oxides into metal hydride and metal alkyl species, especially in materials with co-localized surface acid sites, could lead to unique multifunctional reaction mechanisms. Such organometalloxide catalysts could be particularly interesting for the selective cleavage of carbon–carbon bonds in hydrocarbons, which has traditionally relied on precious metal-catalysed hydrogenolysis[2–4] or acid-catalysed hydrocracking[5]. Moreover, developing more effective processes for conversions of hydrocarbon plastics, which are currently used and discarded on a scale of hundreds of megatons[6], would also benefit from Earth-abundant oxide-based catalysts.

The growing global plastic waste crisis[7] has motivated recent studies of supported precious metal nanoparticles as catalysts for hydrogenolysis of polyolefins[8–12]. Carbon–carbon bond cleavage via organozirconium-mediated β-alkyl elimination[13] has received less attention[14], despite the Earth abundance of Zr and attractive mild conditions (<150 °C and atmospheric pressure) used for the hydrogenolysis of polyolefins in pioneering work by Dufaud and Basset[15]. The combination of a few of the advantageous features of these distinct classes of catalysts may provide an appropriate strategy for designing organozirconia-mediated hydrogenolysis of hydrocarbons.

The conventional strategy to achieve high catalytic activity involving evenly dispersed sites over high-surface-area materials has not yet enabled the activation of metal oxides for hydrogenolysis. An alternative catalyst design instead positions active sites at specific isolated locations within a 3D nanosized architecture. In support of this idea, a mesoporous silica shell/platinum catalyst/silica core ($mSiO_2$/Pt/SiO_2) 3D architecture that isolates small Pt nanoparticles at the bottom of mesoporous wells provides high activity and long catalyst lifetimes in polyolefin hydrogenolysis[16,17]. In contrast, external-facing platinum in Pt/SiO_2 materials readily deactivates by leaching and sintering. The synthetic methods that localize metal nanoparticles in a 3D architecture, however, are not readily adapted to SOMC zirconium complexes due to their unwanted reactivity with air and moisture, which forces the final synthetic step to be organometallic site installation. In that covalent grafting reaction, the placement of sites is governed by the locations of surface hydroxy groups, which are notoriously difficult to control on metal oxide surfaces[18]. Instead, we sought to advance the construction of mixed metal oxide–silica architectures by localizing zirconia particles in a narrow zone within mesoporous silica nanoparticles.

Metal nanoparticle and SOMC catalysts both benefit from coordinatively unsaturated sites, achieved in metal nanoparticle catalysts through high proportions of edge and corner atoms in small nanoparticles and in SOMC catalysts by immobilization onto inert supports. Although zirconia-catalysed polyolefin hydrogenolysis had not previously been demonstrated, zirconia was shown to catalyse the hydrogenation of alkenes[19], and hexane was cracked over zirconia to give similar products and selectivity to the protonated Zeolite Socony Mobil-5 (HZSM-5) acid catalyst[20]. Moreover, tests of zirconia as a support for noble metals in hydrogenolysis also suggested its possible activity[21]. Smaller nanoparticles[22], the presence of oxygen vacancies[20] and undercoordinated sites[23] have also been proposed to enhance the reactivity of zirconia by creating either reducible surface sites or Lewis acid sites[24]. Thus, metal oxides with coordinatively unsaturated surface sites in small nanoparticles that are isolated and stabilized by an inert 3D architecture could be promising for carbon–carbon bond hydrogenolysis.

Herein, we demonstrate that ultrasmall amorphous localized zirconia nanoparticles (L-ZrO_2), covalently embedded in silica and clamped in a void between two mesoporous platelets (L-ZrO_2@$mSiO_2$), are highly active in the hydrogenolysis of polyethylene. The architecture enhances the catalytic activity of zirconia to become comparable to that of Pt/C and improves its selectivity towards liquid products. Spectroscopic and computational studies implicate heterolytic H–H and C–H bond cleavage steps that generate Zr–H, Zr–C and O–H bonds, indicating that organometallic elementary steps are involved in polymer deconstruction and product formation. From a practical perspective, the catalyst can be handled under ambient conditions and provides a competitive, Earth-abundant and low-cost alternative to precious metal hydrogenolysis catalysts for polyolefin deconstruction.

Results

Synthesis and catalyst structure

L-ZrO_2@$mSiO_2$ was designed for zirconium-catalysed polyolefin deconstruction (Figs. 1 and 2). Ultrasmall $ZrO_x(OH)_{4-2x}$ nanoparticles were dispersed on graphene oxide sheets (Supplementary Fig. 1), $mSiO_2$ layers were grown on the $ZrO_x(OH)_{4-2x}$/graphene oxide and the resulting material was washed and calcined to remove structure-directing agents. Inductively coupled plasma mass spectrometry (ICP-MS) analysis of L-ZrO_2@$mSiO_2$ revealed a ZrO_2 loading of 4.7 wt% (Supplementary Table 1). ICP-MS analyses of three batches of as-synthesized L-ZrO_2@$mSiO_2$ catalysts (Supplementary Table 2) ruled out the presence of any other transition metals in the catalyst, including Ru, Rh, Pt, Pd, Au, Re, Os, Ir, Ni, Fe, Co, Cu, Zn, Mo, W, Cd, Ce, Hf, Ti and V. The elemental purity of L-ZrO_2@$mSiO_2$ was further supported by X-ray photoelectron spectroscopy (Supplementary Fig. 2) and energy dispersive X-ray spectroscopy (Supplementary Fig. 3).

The performance of L-ZrO_2@SiO_2 is best understood through comparisons with the behaviour of several reference catalysts, whose relevant structures are briefly described here and summarized in Supplementary Table 1. $mSiO_2$, synthesized by templated silica growth on graphene oxide[25,26], has the same layered platelet morphology and porous structure (Supplementary Fig. 4) as L-ZrO_2@$mSiO_2$. Imp-ZrO_2/$mSiO_2$, produced by incipient wetness impregnation of zirconium precursors into $mSiO_2$, contains randomly dispersed amorphous ZrO_2 nanoparticles (Supplementary Fig. 5). ZrO_2-6/$mSiO_2$ was prepared by immobilizing pre-synthesized 6 nm monoclinic ZrO_2 nanoparticles (Supplementary Fig. 6) on the external surface of $mSiO_2$ (Supplementary Fig. 7). ZrO_2-30 and Pt/C are, respectively, commercial monoclinic zirconia (~30 nm in size) and platinum nanoparticles supported on carbon (1.3 ± 0.4 nm in size) (Supplementary Fig. 8). L-Pt@$mSiO_2$ (Supplementary Fig. 9), synthesized by deposition of $PtO_x(OH)_{4-2x}$

https://doi.org/10.1038/s41929-023-00910-x

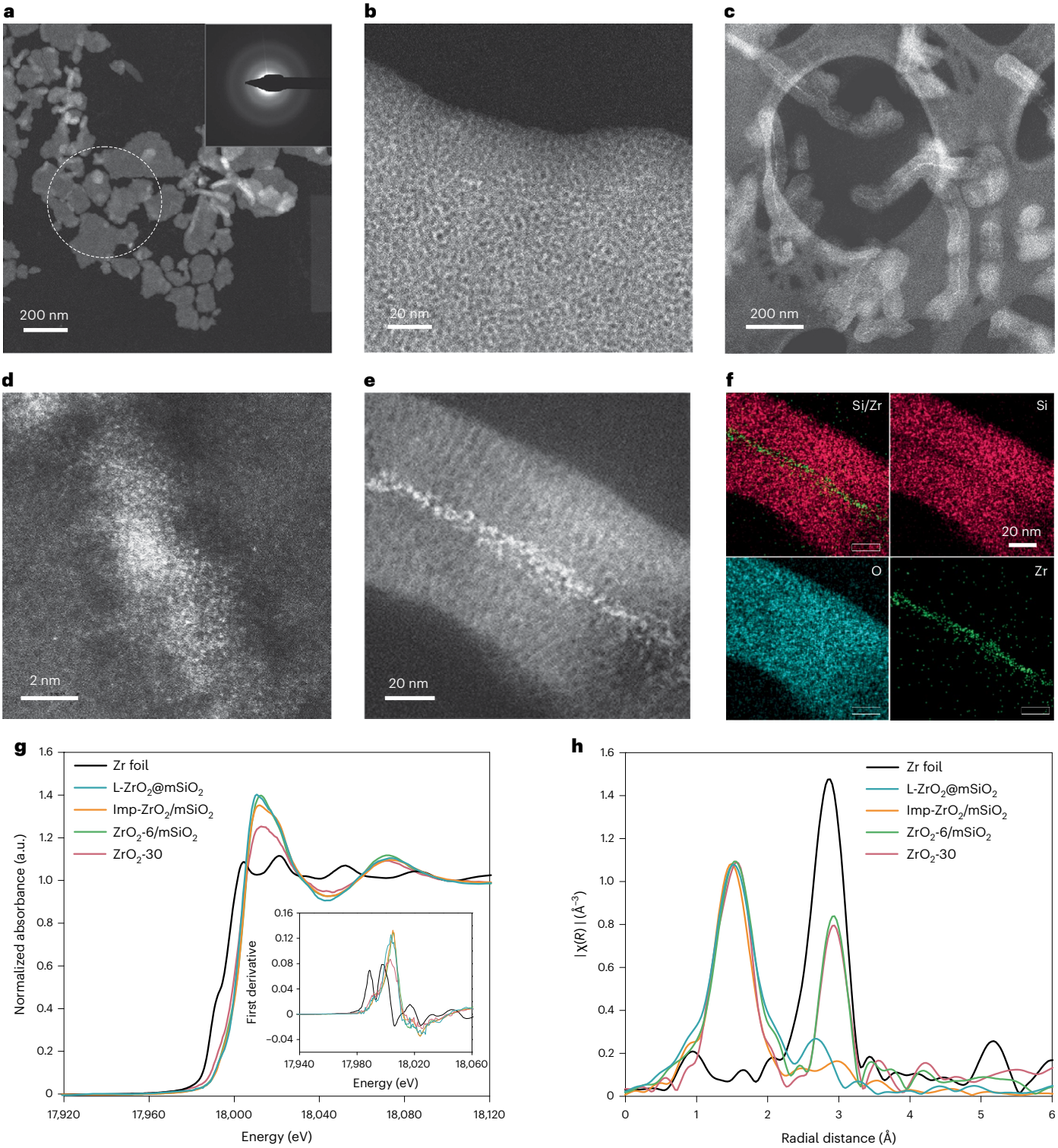

Fig. 2 | Electron microscopy and X-ray absorption spectroscopy for ZrO_2 catalyst characterization. a,**b**, Low-magnification (**a**) and high-magnification (**b**) high-angle annular dark-field (HAADF) STEM images of L-ZrO_2@mSiO_2. Inset in **a**, selected area electron diffraction pattern. **c**,**d**, Low-magnification (**c**) and high-resolution (**d**) HAADF STEM images of the cross-section of an L-ZrO_2@mSiO_2 particle prepared by microtomy. **e**,**f**, High-magnification HAADF STEM image (**e**) and corresponding energy dispersive X-ray spectroscopy elemental (top left, Si and Zr; top right, Si; bottom left, O; bottom right, Zr) maps (**f**) of the cross-section of an L-ZrO_2@mSiO_2 particle. **g**,**h**, Normalized Zr *k*-edge X-ray absorption near-edge structure spectra (**g**) and k_2-weighted EXAFS spectra (**h**) of L-ZrO_2@mSiO_2 and control samples. Inset in **g**, first derivative spectra.

nanoparticles on graphene oxide (Supplementary Fig. 10) followed by growth of the mSiO_2 shell, creates a comparable architecture to L-ZrO_2@mSiO_2 with 3.5 ± 0.8 nm platinum nanoparticles instead of zirconia. The total surface area and Barrett–Joyner–Halenda pore size for mSiO_2-based samples are ~900–1,000 $m^2\ g^{-1}$ and 3.4–3.8 nm, respectively (Supplementary Table 1).

The low-magnification scanning transmission electron microscopy (STEM) image (Fig. 2a) of L-ZrO_2@mSiO_2 showed its separated

nanoplatelet particle morphology, with lateral dimensions ranging from hundreds of nanometres to a few micrometres. Pore diameters of 3.4 ± 0.4 nm in the mesoporous silica nanoplatelets, as revealed by the higher-magnification image (Fig. 2b), matched the values obtained with N_2 sorption isotherm measurements (Supplementary Table 1 and Supplementary Fig. 11). Notably, the STEM images of cross-sectioned L-ZrO_2@mSiO_2 particles, prepared with an ultramicrotome (Fig. 2c–e), clearly showed a thin (~3 nm) bright band, as was identified by elemental mapping as a region of concentrated zirconium (Fig. 2f), between the two 35-nm-thick sheets of mSiO_2. The mesopores in mSiO_2 are aligned perpendicular to the nanoplate (Fig. 2e)[26,27], and the diameter of the ZrO_2 particles is 3.0 ± 0.5 nm (Supplementary Fig. 12).

The amorphous nature and chemical structure of the ultrasmall ZrO_2 nanoparticles in L-ZrO_2@mSiO_2 were established by electron diffraction, powder X-ray diffraction, X-ray absorption spectroscopy and solid-state nuclear magnetic resonance (NMR) spectroscopy. A diffuse ring in the selected area electron diffraction pattern (inset in Fig. 2a) indicated amorphous characteristics of the material, in contrast with the sharp diffraction spots or rings typical of crystalline substances. The high-resolution image (Fig. 2d) further revealed that both ZrO_2 and mSiO_2 lack long-range order. Diffraction peaks from ZrO_2 were not detected in the powder X-ray diffraction pattern of L-ZrO_2@mSiO_2 (Supplementary Fig. 13). The strong pre-edge peak in X-ray absorption near-edge structure spectra (Fig. 2g) and the same peak intensity in Fourier-transformed extended X-ray absorption fine-structure (EXAFS) spectra (Fig. 2h) for the Zr–O distance in all ZrO_2 samples confirmed that Zr is in the +4 oxidation state. The non-crystalline nature of ZrO_2 in L-ZrO_2@mSiO_2 was distinguished by EXAFS from crystalline ZrO_2-6/mSiO_2 and ZrO_2-30, which contained a Zr–Zr scattering path at 2.9 Å.

The direct ($e \rightarrow {}^{17}O$) dynamic nuclear polarization (DNP) surface-enhanced (SENS)[28] magic angle spinning (MAS) ^{17}O Hahn echo NMR spectrum of L-ZrO_2@mSiO_2 (Fig. 3a) contained a broadened, axially symmetric, quadrupolar powder pattern with an isotropic chemical shift of 50 ppm and a quadrupolar coupling constant of 5 MHz, assigned to siloxane linkages. To aid in the assignment of additional broad signals at 400 and 150 ppm at 9.4 T, probably attributable to the ZrO_2 nanoparticles, we acquired DNP SENS data on pure monoclinic ZrO_2 nanoparticles (Fig. 3b). ZrO_2-30 gave rise to sharp resonances at 325 and 402 ppm from μ^4-O^{2-} and μ^3-O^{2-} lattice sites[29] and a broad resonance from approximately 425–300 ppm from surface μ^3- and μ^4-O^{2-} sites. The resonance at 400 ppm in the ^{17}O Hahn echo spectrum of L-ZrO_2@mSiO_2 was assigned to disordered surface Zr oxide sites. In addition, the sharp signals from the crystalline ZrO_2 phase contrasted the broad resonances from L-ZrO_2@mSiO_2, further supporting the conclusion that the ZrO_2 particles are amorphous. We further performed indirect ($e \rightarrow {}^{1}H \rightarrow {}^{17}O$) DNP SENS experiments to assign the resonance at 150 ppm in L-ZrO_2@mSiO_2, using phase-shifted recoupling effects a smooth transfer of order (PRESTO) experiments to acquire the ^{17}O MAS NMR spectra of only the hydroxy species[30]. The PRESTO spectrum of L-ZrO_2@mSiO_2 (Fig. 3c) was dominated by a previously obscured resonance at approximately −50 ppm assigned to surface silanols. Alternatively, the spectrum of ZrO_2-30 contained a signal at approximately 150 ppm at 9.4 T (Fig. 3d), which was unambiguously assigned to Zr–OH sites[29]. The contrast between the spectra of the two samples suggests that a dominant component of the resonance at 150 ppm in the ^{17}O Hahn echo spectrum of L-ZrO_2@mSiO_2 is not a Zr–OH species but rather Si–O–Zr linkages. We observed such a site in a previous study of a Zr(NMe_2)$_3$/SiO_2 species where it resonated at 146 ppm at 9.4 T[31]. Importantly, the observation of this resonance confirms that the silica and zirconia phases are covalently linked to one another.

The thermochemical stability of ZrO_2 is affected by the mSiO_2 shell. Calcination of $ZrO_x(OH)_{4-2x}$/graphene oxide at 550 °C formed a mixture of tetragonal and monoclinic ZrO_2 nanocrystals (Scherrer size = 5.5 and 9.3 nm, respectively; Supplementary Fig. 14). Similar calcination of L-ZrO_2@mSiO_2 did not provide detectable signals of crystalline

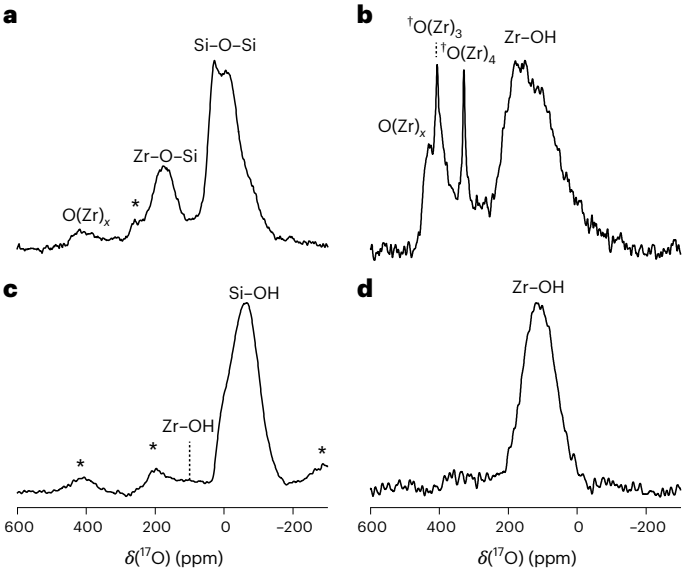

Fig. 3 | Solid-state NMR spectra of ZrO_2 catalysts. a,b, Direct DNP-enhanced ^{17}O Hahn echo spectra of L-ZrO_2@mSiO_2 (**a**) and monoclinic ZrO_2-30 nanoparticles (**b**). **c,d**, Indirect DNP-enhanced $^{17}O\{^1H\}$ PRESTO NMR spectra of L-ZrO_2@mSiO_2 (**c**) and ZrO_2-30 nanoparticles (**d**). All of the data were acquired at a MAS rate of 14 kHz. Spinning sidebands are indicated by asterisks. Crystalline sites are further labelled by daggers.

domains (Supplementary Fig. 13). It is likely that the confinement of ultrasmall ZrO_2 nanoparticles within the mesopores, along with the covalent Si–O–Zr bonding, limits their growth and crystallization.

Polymer deconstruction catalysis

Polyethylene hydrogenolysis was performed with ~3 g melted polyethylene (number-averaged molecular mass (M_n) = 20 kDa and weight-averaged molecular mass (M_w) = 91 kDa; Supplementary Fig. 16) and 5.5 mg catalyst under 0.992 MPa of H_2 at 300 °C as the standard conditions. The high mass-specific catalytic activity of L-ZrO_2@mSiO_2 was established by the rate of C–C bonds cleaved per metal mass (2.3 ± 0.4 mol H_2 (g Zr)$^{-1}$ h^{-1}). The number of C–C bonds that were broken in each experiment was determined by measuring the consumption of H_2 (each H_2 molecule consumed corresponds to one hydrogenolysed C–C bond) and comparing starting and final total molecular weight distributions (M_n) of the entire sample, including the C_1–C_9 species in the reactor headspace, the C_8–C_{50} liquid and wax fraction extracted with dichloromethane and the >C_{50} polymeric solid residue (Fig. 4a,b and Supplementary Tables 3 and 6). The M_n versus time curve followed the generally expected decay (Supplementary Fig. 15).

A few zirconia materials show catalytic activity in polyethylene hydrogenolysis, with L-ZrO_2@mSiO_2 providing the highest conversion of polyethylene and high mass-specific activity for C–C bond breakage (Fig. 4c). Its activity for C–C bond cleavage is ~23 ± 2× and 2.4 ± 0.3× higher than the activities of ZrO_2-30 and ZrO_2-6/mSiO_2, and comparable to that of Imp-ZrO_2/mSiO_2 (Supplementary Table 6). Remarkably, the activity of L-ZrO_2@mSiO_2 for C–C cleavage is even competitive with that of Pt-based catalysts following the trend L-ZrO_2@mSiO_2 ~ Pt/C < L-Pt@mSiO_2. The similar activity of Pt and confined Zr, along with the <0.001 wt% concentration of other transition metals measured by ICP-MS of as-synthesized and post-reaction zirconia catalysts, as well as catalyst-free control experiments, also ruled out trace contaminants as being catalytically important species.

The L-ZrO_2@mSiO_2-catalysed polyethylene hydrogenolysis produced a narrow, Gaussian-type C_{18}-centred distribution of liquid hydrocarbons, with C_9–C_{27} representing >90% of the chains. This

https://doi.org/10.1038/s41929-023-00910-x

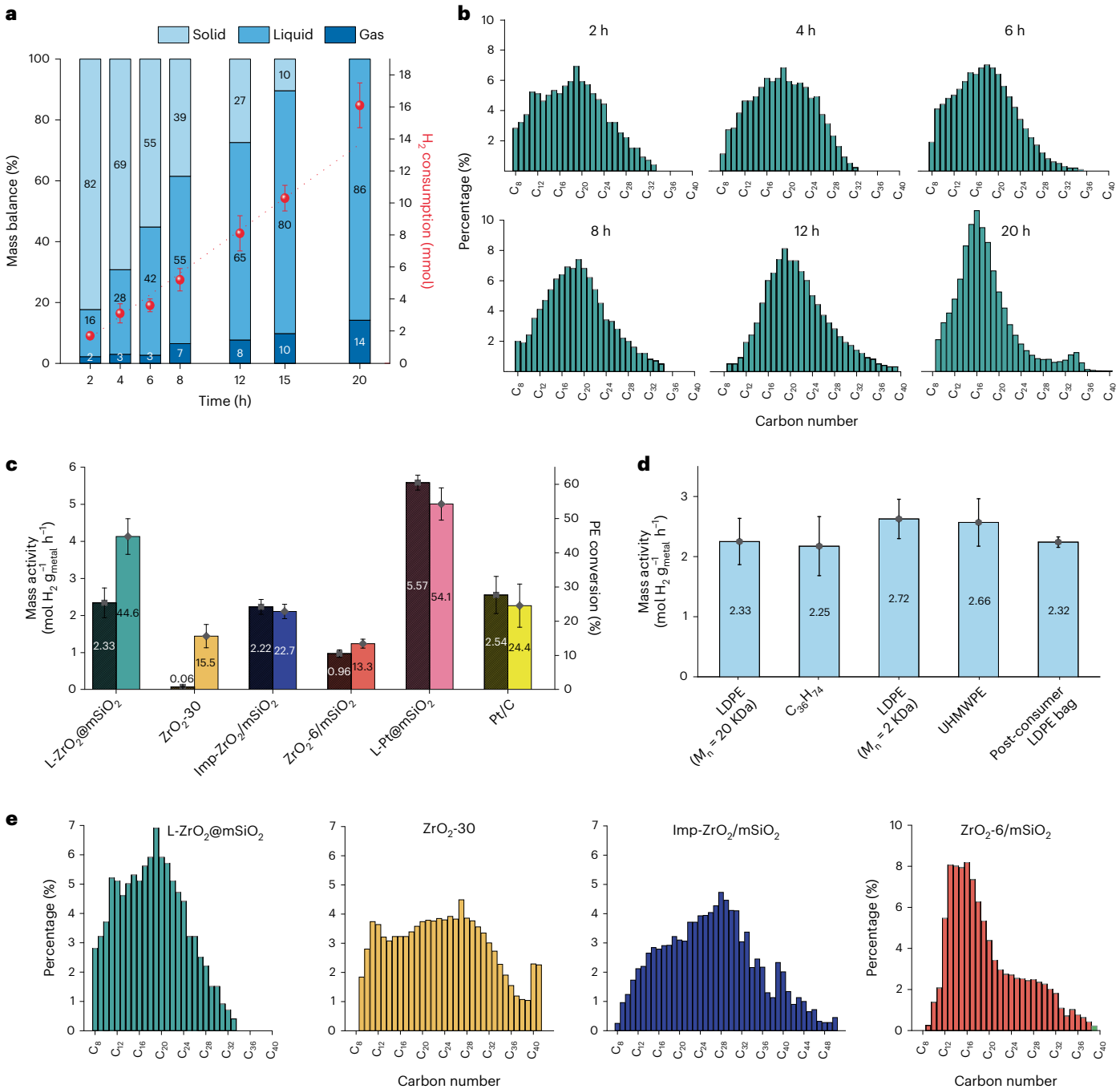

Fig. 4 | Hydrogenolysis results from L-ZrO_2@$mSiO_2$ and control catalysts. **a**, Time-dependent conversion of polyethylene (M_n = 20 kDa; M_w = 90 kDa; $Đ$ = 4.8), liquid yield and volatile yield, in mass percentage, catalysed by L-ZrO_2@$mSiO_2$ under H_2 at 300 °C. The data are presented as H_2 quantification (means ± 1σ), as determined from three or more gas chromatography measurements. **b**, Carbon number distribution of liquid products from the hydrogenolysis of polyethylene catalysed by L-ZrO_2@$mSiO_2$ after 2, 4, 6, 8, 12 and 20 h. **c**, Comparison of C–C bond cleavage activity (left axis, hashed bars, mean ± 1σ, as determined from three H_2 quantification measurements and the mass of metal loading) and conversion of polyethylene (PE; right axis, open bars, mean ± 1σ, as determined from two experiments of isolated material) at 300 °C for 6 h. **d**, Comparison of C–C bond cleavage reactivity for short, long, and ultra-high-molecular-weight high-density polyethylene (UHMWPE), as well as linear and branched polymers in L-ZrO_2@$mSiO_2$-catalysed hydrogenolysisσ (mean ± 1σ). **e**, Carbon number distribution of liquid products catalysed by L-ZrO_2@$mSiO_2$, ZrO_2-30, Imp-ZrO_2/$mSiO_2$ and ZrO_2-6/$mSiO_2$, obtained from reactions that consumed similar moles of H_2.

characteristic distribution was formed at the initial stage of the reaction and increased in yield in a roughly linear fashion until ~75% polyethylene conversion (Fig. 4a,b and Supplementary Table 3). The volatile species, which represented the low-end tail of the product distribution, similarly increased in yield as the reaction progressed (Supplementary Figs. 20–44). After >80% conversion of the polyethylene, the average chain length in the liquid products decreased to C_{16} after 15 h (Supplementary Figs. 47 and 48) and sharpened after 20 h (Fig. 4b), and the weight fraction of volatile products, mostly composed of methane and ethane, further increased (Supplementary Figs. 45–53). We attribute these observations to the secondary hydrogenolysis of the C_{18}-centred distribution that occurred primarily at the ends of the chains. These results further indicate that L-ZrO_2@$mSiO_2$-catalysed hydrogenolysis is selective for the long hydrocarbon chains of polyethylene rather than the

shorter chains of the primary products. This remarkable behaviour resembles $mSiO_2$/Pt/SiO_2-catalysed hydrogenolysis of polyethylene[16,17] and contrasts with the performance of the other ZrO_2 catalysts, which give broader, non-Gaussian or multimodal distributions (Fig. 4e), which also vary throughout the polyethylene conversion (Supplementary Tables 4 and 6 and Supplementary Figs. 54–87).

This highly disperse polyethylene (M_n = 20 kDa) represents the typical range used for flexible packaging applications. Accordingly, L-ZrO_2@$mSiO_2$-catalysed hydrogenolysis of a post-consumer low-density polyethylene (LDPE) grocery bag (M_n = 10.6 kDa and M_w = 150 kDa; dried under vacuum; Supplementary Fig. 18) resulted in equivalent reactivity (Fig. 4d; 2.3 ± 0.4 mol H_2(g Zr)$^{-1}$ h^{-1}). The catalytic activity was also similar for hexatriacontane (n-$C_{36}H_{74}$), LDPE (M_n = 2.8 kDa and M_w = 5.3 kDa; Supplementary Fig. 17) and ultra-high-molecular-weight high-density polyethylene (M_w = ~3,000–5,000 kDa). These results suggest that rates of threading of chains into pores and translocation to the active sites at the ends of the pores are not limiting the rates of C–C bond cleavage for short and long chains as well as branched and linear polymers, and the distribution is independent of the C–C bond cleavage rate; however, the conformations of long and short chains probably vary to influence the distributions. Specifically, hydrogenolysis of hexatriacontane provided a distribution of chain end-cleaved hydrocarbons, similar to the process observed for secondary hydrogenolysis of C_{18} primary products noted above. In contrast, ultra-high-molecular-weight high-density polyethylene or post-consumer LDPE gave broad distributions, respectively (Supplementary Figs. 88–103). In addition, L-ZrO_2@$mSiO_2$ produced a narrower distribution of chain lengths of extractable species compared with the other ZrO_2-based catalysts at a similar polyethylene conversion (39–54%; Fig. 4e).

Mechanistic analysis

The amorphous ZrO_2 nanoparticles in L-ZrO_2@$mSiO_2$, leading to low-coordinated metal ions[32–35], were modelled by a Zr adatom supported on a (−111) surface of monoclinic ZrO_2 (Zr/ZrO_2). A constrained ab initio thermodynamic analysis of 21 structures (Supplementary Fig. 106 and Supplementary Table 9) with varying numbers of H, O and OH groups adsorbed on the Zr atom identified $Zr(O)_2$/ZrO_2 as the lowest energy of a possible adatom species with reference to Zr/m-ZrO_2, gas-phase H_2 and trace H_2O (**a0** in Fig. 5; ΔG = −3.41 eV; T = 300 °C; P_{H_2} = 0.90 MPa; P_{H_2O} = 6.89 × 10^{-15} MPa). In $Zr(O)_2$/ZrO_2, the Zr adatom is bonded to two oxo species with short Zr–O interatomic distances (1.92 and 1.97 Å) and coordinated by surface oxygen donors with longer Zr–O distances. The oxo species are also bridged to the Zr of the support. The resulting electron-deficient, low-coordinate Zr species are representative of adatom, corner and edge sites that are expected to be widely present in the amorphous ZrO_2 nanoparticles. The $Zr(O)_2$/ZrO_2 species reacts with H_2 via heterolytic dissociation, leading to HZr(OH)(O)/ZrO_2 (ΔG = −3.34 eV; **b0** in Fig. 5 and Supplementary Table 9).

This heterolytic dissociation of H_2 on L-ZrO_2@$mSiO_2$ was supported by in situ diffuse reflectance infrared Fourier transform spectroscopy experiments under flowing H_2 at 300 °C, which revealed a small peak at 1,547 cm^{-1}, bands at 3,731 and 1,613 cm^{-1} and a broad feature at 3,600–3,100 cm^{-1} (Supplementary Fig. 104). The signal at 1,547 cm^{-1} disappeared upon flowing D_2; however, the expected band at ~1,100 cm^{-1} was not detected above the strong silica absorption (Supplementary Fig. 105). The peak intensities at 3,730 and 3,600–3,100 cm^{-1} also diminished under D_2, and signals appeared at 2,700 and 2,600–2,300 cm^{-1}. These signals disappeared and the original features reappeared upon flowing H_2. On the basis of this H/D exchange behaviour and reported assignments[36,37], the band at 1,547 cm^{-1} was assigned to ν_{ZrH} and the other signals were attributed to ν_{OH} from SiOH and ZrOH, providing experimental support for the idea of heterolytic dissociative adsorption of H_2 and D_2 in L-ZrO_2@$mSiO_2$.

Low-energy pathways were investigated computationally using density functional theory (DFT), and several plausible models for hydrogenolysis of n-hexane by the $Zr(O)_2$/ZrO_2 species at 300 °C under 0.1 MPa of H_2 are presented here (Fig. 6). Although the experimental study focused primarily on polyethylene, the secondary cleavage of the C_{18}-centred primary products and hydrogenolysis of hexatriacontane indicate that L-ZrO_2@$mSiO_2$ is also a catalyst for small-molecule hydrogenolysis. Hexane and the low-coordinated $Zr(O)_2$ react through an initial C–H bond activation to form $H_{13}C_6$-Zr(O)(OH)/ZrO_2 (**a1** → **a2**), involving transfer of a hexane H atom to one of the O atoms and the hexyl group to the Zr atom. This step, as well as the heterolytic H_2 cleavage above, is reminiscent of 1,2-addition of a C–H or H–H bond across Zr=NR to give C–Zr–NHR or H–Zr–NHR[38,39]. Hexane metalation by HZr(OH)(O)/ZrO_2 to give $H_{13}C_6$-Zr(O)(OH)/ZrO_2 with liberation of H_2 (**b1** → **a2**), similar to the σ-bond metathesis reaction of $(SiO)_3ZrH$ and hydrocarbons[15], is ruled out by its 0.5 eV higher barrier than that of hexane dissociative adsorption on $Zr(O)_2$/ZrO_2.

Kinetically favourable cleavage of the β-C–H bond in $H_{13}C_6$-Zr(O)(OH)/ZrO_2 produces *cis*-2-hexene (**a2** → **c1**; G^{act} = 0.94 eV), 1-hexene or *trans*-2-hexene (via a <0.3 eV higher barrier compared with *cis*-2-hexene). Alternatively, the 1.26 eV barrier for β-C–C bond cleavage in $H_{13}C_6$-Zr(O)(OH)/ZrO_2 to give **a3** is slightly higher. After hydrogenation of the propene product to propane, this pathway is thermodynamically more favourable than the endergonic formation of *cis*-2-hexene. Our calculations predicted a free energy of 1.8 eV for the C–C bond cleavage transition state over the $Zr(O)_2$ model, which is the highest-energy state in the free energy profiles of $Zr(O)_2$ active site models (Fig. 6). Thus, this process could be rate limiting for n-hexane and possibly also polyethylene hydrogenolysis. In addition, C–H or C–C bond cleavage steps solely based on acidic Zr(OH) have much higher activation barriers (G^{act} = 2.05 and 2.30 eV, respectively) than 1,2-addition and β-elimination. A bona fide acid catalyst, beta zeolite, under the standard hydrogenolysis condition gave coke and branched products in experiments using polyethylene. The differences between acid- and L-ZrO_2@$mSiO_2$-catalysed deconstructions further support the organozirconia-catalysed computational mechanism.

Propane is eliminated by a proton transfer from the proximal hydroxy to the propylzirconium species to regenerate the $Zr(O)_2$ species; the protonolytic propane elimination distinguishes this pathway from the σ-bond metathesis mechanism typically proposed for reactions of H_2 and molecular organozirconium compounds in solution. The activation barrier for an alternative mechanism involving the σ-bond metathesis-type reaction of H_7C_3–Zr(O)(OH) and H_2, as established for catalytic alkene hydrogenation or alkane hydrogenolysis by seemingly related SOMC species $(\equiv SiO)_3ZrH$[40], is ~0.4 eV higher than protonolytic elimination and appears less likely. In support of this idea, the reaction of grafted $\equiv Si–O–Zr(CH_2CMe_3)_3$ and H_2 requires several hours at 150 °C. Although the hydridozirconium species H–Zr(O)OH is neither involved in C–H bond metalation nor formed from H_7C_3–Zr(O)(OH) and H_2, it is nonetheless essential for hydrogenation of propene (**a5** → **a7**).

These reaction steps were confirmed by parahydrogen (pH_2)-induced polarization (PHIP) NMR spectroscopy, a technique that produces NMR signal enhancements only when the hydrogenation with pH_2 occurs by pairwise addition. The ^{1}H PHIP NMR spectrum for L-ZrO_2@$mSiO_2$-catalysed propene hydrogenation under ALTADENA (adiabatic longitudinal transport after dissociation engenders net alignment)[41] conditions using 99% pH_2 (Supplementary Fig. 108) showed net alignment multiplet patterns of the CH_2 and CH_3 peaks with integral ratios close to 1:−1. Thus, the propane product had received both protons from the same pH_2 molecule with retention of spin–spin coupling[42], in accordance with the steps **a5** → **a7**. The σ-bond metathesis reaction of H_2 and propylzirconium transfers only a single proton from a pH_2 molecule and cannot produce the NMR signal enhancements in accordance with the above calculations. Moreover, 1,2-addition of the hydrocarbon CH bond (for example, **a1** → **a2**) is the reverse reaction

https://doi.org/10.1038/s41929-023-00910-x

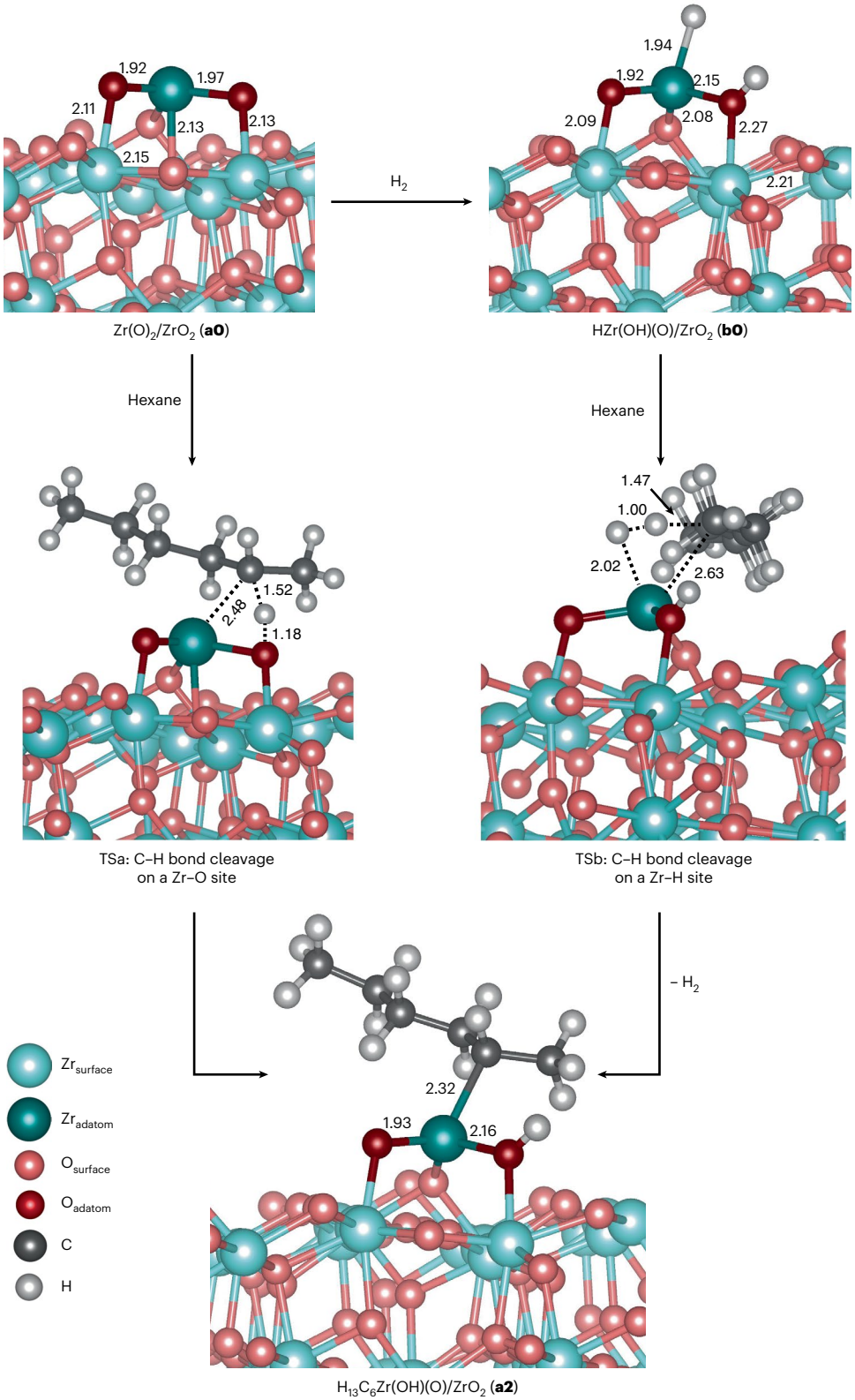

Fig. 5 | Calculated bond activation by ZrO_2. Side views of the optimized structures of intermediates and transition states (TS) corresponding to the initial C–H bond activation of hexane over $Zr(O)_2/ZrO_2$ (**a0**) and $HZr(OH)(O)/ZrO_2$ (**b0**) adatom models, both forming $H_{13}C_6Zr(OH)(O)/ZrO_2$ (**a2**). Distances are given in Å.

of propane elimination, by H transfer from OH to propylzirconium (**a6** → **a7**). The principle of microscopic reversibility and the PHIP results together indicate that hydrocarbon metalation on L-ZrO_2@mSiO_2 is more consistent with 1,2-addition than dehydrogenative metalation by σ-bond metathesis, again in line with the calculations.

A microkinetic model was used to further examine the *n*-hexane hydrogenolysis over the $Zr(O)_2$/m-ZrO_2 active site, employing a continuous stirred-tank reactor (CSTR; $T = 300$ °C; $P_{H_2} = 1$ MPa; $P_{hexane} = 0.1$ MPa; Table 1). The model revealed that as hexane conversion increases with increased residence time, selectivity for the C–C bond cleavage

https://doi.org/10.1038/s41929-023-00910-x

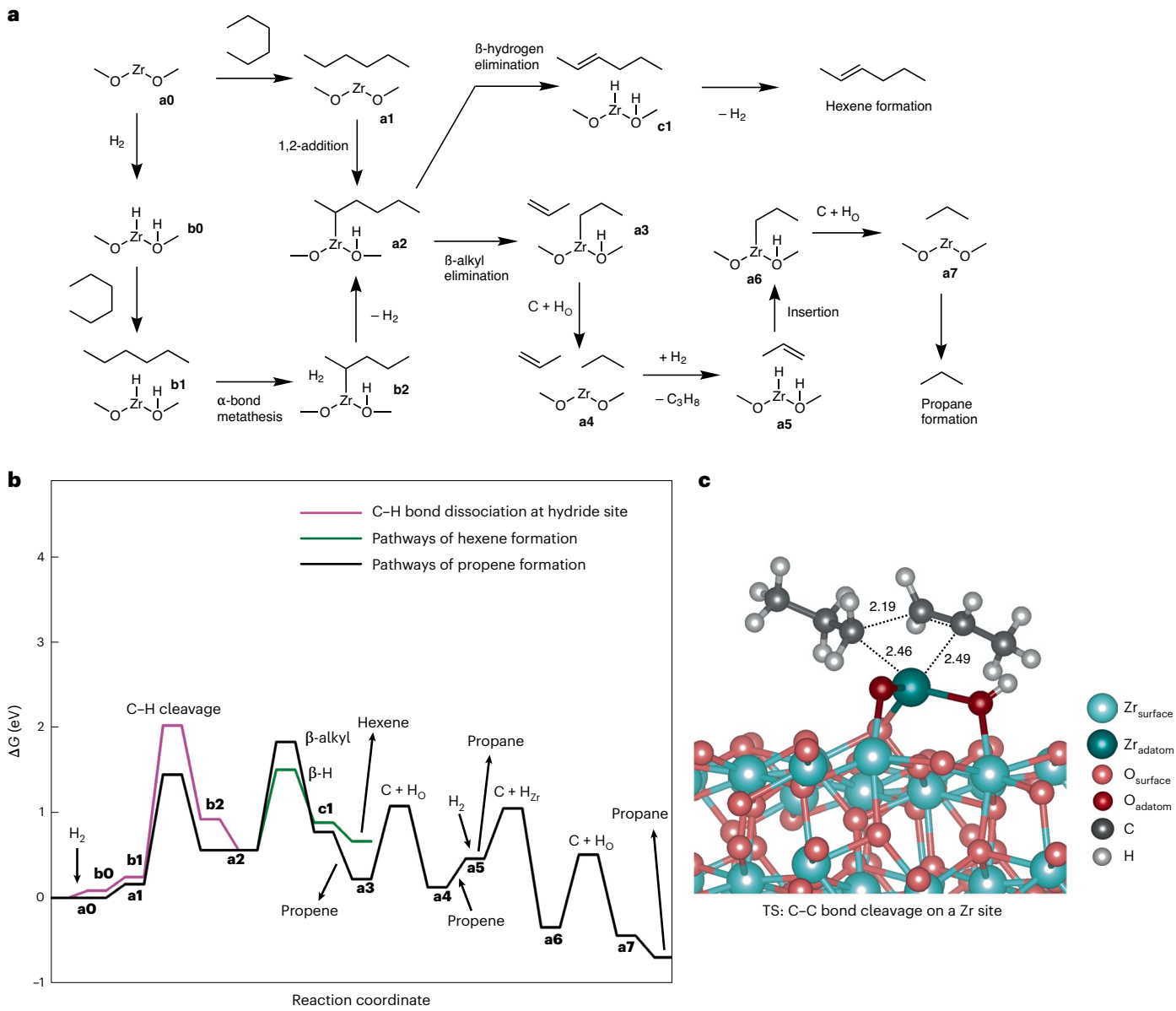

Fig. 6 | Calculated mechanistic model for hydrocarbon hydrogenolysis. a, Schematic of the reaction pathways considered for *n*-hexane hydrogenolysis on the $Zr(O)_2$/m-ZrO_2 and H–Zr(O)(OH)/m-ZrO_2 models. **b**, Corresponding free energy profiles (T = 300 °C; P_{gas} = 0.1 MPa). All free energies are with reference to the sum of the energies of the $Zr(O)_2$/m-ZrO_2 catalyst model and the reactant gas molecules. **c**, Transition state calculated for C–C bond dissociation.

product, propane, increases to 100% at sufficiently high residence times. These results suggest that the C–C bond cleavage is favoured in the presence of H_2, which shifts the equilibria towards the propane formation. The microkinetic model also predicted a high steady-state surface coverage of H–Zr(O)OH (θ = 0.63) under H_2 (1 MPa), which further promoted the conversion of propene to propane. Reasonable turnover frequencies, on the order of 10^{-4} s^{-1}, were observed in the microkinetic model when hexane conversion to propane was between 0.1 and 12.4%.

The activation barriers of H_2 dissociation and the rate-limiting C–C bond cleavage calculated from the $Zr(O)_2$/m-ZrO_2 model were compared with those from the most stable flat surfaces of monoclinic ZrO_2 (−111) and tetragonal ZrO_2 (101) surface sites (Supplementary Fig. 107). H_2 activation was found to be thermodynamically less favourable on the flat surfaces compared with the $Zr(O)_2$/m-ZrO_2 model. The C–C bond cleavage barriers on the flat surfaces are in the range of 2.1–2.4 eV, in contrast with 1.26 eV for low-coordinated Zr sites, indicating that flat crystal surfaces of ZrO_2 are less active for breaking the C–C bonds of hydrocarbons. Thus, these results are consistent with the experimental observation that ultrasmall amorphous ZrO_2 nanoparticles are more active in polyethylene hydrogenolysis than larger crystalline ZrO_2 nanoparticles dominated by more stable flat surfaces.

Conclusions

Our synthetic, spectroscopic and mechanistic investigations of L-ZrO_2@mSiO_2 reveal the combined architectural and chemical features that enable Earth-abundant, non-reducible metal oxides (Zr, Si and O) to catalyse the selective hydrogenolysis of hydrocarbon polymers. The synthesis of L-ZrO_2@mSiO_2 shows, remarkably, that $ZrO_x(OH)_{4-x}$ nanoparticles are stable under the hydrolytic conditions necessary for the growth of mesoporous silica and creation of the catalytic architecture with core-localized nanoparticles. Moreover, the coordinatively unsaturated surface sites needed for catalysis are stabilized by covalently embedding the amorphous zirconium nanoparticles in the walls

Table 1 | Conversion, selectivity and turnover frequencies of *n*-hexane hydrogenolysis predicted by the microkinetic CSTR model for the $Zr(O)_2$/m-ZrO_2 active site with respect to the effective residence time[a]

Effective residence time ($\alpha\times\tau$) (s)	Conversion (%)	Selectivity (%)			Turnover frequency (s^{-1})[b]
		Hexene	Propane	Propene	
Initial	–	100	3×10^{-2}	3×10^{-2}	4×10^{-1}
10^{-6}	6×10^{-6}	98	2	1×10^{-1}	6×10^{-3}
10^{-4}	3×10^{-5}	42	58	4×10^{-2}	2×10^{-4}
10^{-2}	1×10^{-3}	9×10^{-1}	99	7×10^{-4}	1×10^{-4}
1	1×10^{-1}	9×10^{-3}	100	8×10^{-6}	1×10^{-4}
10^{2}	12	9×10^{-5}	100	2×10^{-6}	1×10^{-4}
10^{4}	94	9×10^{-7}	100	1×10^{-6}	9×10^{-6}

[a](T = 300 °C; P_{H_2} = 1 MPa; P_{hexane} = 0.1 MPa). [b]The expected turnover frequency uncertainties are 2–3 orders of magnitude due to the expected DFT uncertainties of 0.2–0.3 eV.

of mesoporous silica. These sites, modelled as $Zr(O)_2$ surface species in DFT calculations, mediate C–C bond hydrogenolysis with comparable activity to Pt/C. The quantitative comparison of activity across a series of catalysts is based on H_2 consumption or the relationship between the number of C–C bonds that are cleaved and the change in M_n of the entire hydrocarbon population, as determined from the detailed characterization of gas, liquid and solid compositions. This quantitative comparison reveals that the catalytic enhancement observed with L-ZrO_2@$mSiO_2$ is more than simply the combination of small crystalline ZrO_2 with $mSiO_2$, as shown by the poorer activity of ZrO_2–6/$mSiO_2$.

In addition, L-ZrO_2@$mSiO_2$ provides advantageous selectivity over the other zirconia-based catalysts investigated in this study. Alignment of long chains in the pores[16], non-dissociative adsorption of polymer onto the walls of silica and escape of smaller products through the void space between the two mesoporous silica plates may all contribute to higher selectivity. In fact, both L-ZrO_2@$mSiO_2$ and L-Pt@$mSiO_2$ have sites localized at the ends of mesopores and are both more selective than their non-pore-confined analogues. The mechanisms of zirconia- and platinum-catalysed reactions, however, are distinct. In fact, the energetically favourable heterolytic mechanism for H–H and C–H bond cleavage on $Zr(O)_2$/ZrO_2 is different from those proposed for reducible oxides or metal nanoparticles, or even the SOMC zirconium hydride, instead resembling 1,2-addition to zirconium imido compounds. This heterolytic cleavage generates O–H and Zr–H or Zr–CH_2CH_2R species, which subsequently engage in protonolytic elimination, insertion and β-alkyl elimination. Thus, the proposed active species is a bifunctional (hydroxy)organozirconium oxide species. Access to such species directly from ZrO_2, rather than by grafting neopentylzirconium onto silica, allows the catalytic architecture to be constructed under aqueous conditions and enables the catalytic chemistry to be accessed with air-stable precursors. In this sense, hydrogenolysis with L-ZrO_2@$mSiO_2$ is a previously unrecognized heterogeneous analogue of the SOMC-catalysed C–C cleavage processes.

Methods

Synthesis of L-ZrO_2@$mSiO_2$

L-ZrO_2@$mSiO_2$ was prepared via a two-step synthesis method. In the first step, precipitated zirconium oxyhydroxide nanoparticles were deposited onto graphene oxide in an aqueous solution to give $ZrO_{2-x}(OH)_{2x}$/graphene oxide. That material was prepared as follows. Urea (0.150 g) was dissolved in deionized H_2O (100 ml), graphene oxide (10 mg) was added and the mixture was treated in an ultrasonication bath for 30 min. An aqueous solution of $ZrCl_4$ (0.024 g in 1.25 ml H_2O) was added dropwise to the graphene oxide suspension and the mixture was stirred for 3 h at room temperature. The mixture was subsequently stirred and heated at 90 °C for 12 h. The solid $ZrO_x(OH)_{4-2x}$/graphene oxide product was collected by centrifugation, washed with deionized H_2O (3 × 50 ml) and then dispersed into H_2O (10 ml). In the second step, mesoporous silica ($mSiO_2$) layers were grown onto $ZrO_x(OH)_{4-2x}$/graphene oxide following the procedure described in Supplementary Information for the synthesis of $mSiO_2$ platelets. The final product was characterized and displayed a double-layered platelet structure with ultrasmall ZrO_2 nanoparticles in the narrow core.

Catalytic hydrogenolysis

The catalytic hydrogenolysis of polyolefins was performed in a glass-lined high-pressure autoclave reactor (250 ml; Parr Instruments) equipped with a mechanical impeller-style stirrer and a thermocouple that extended into the melted polymer[16]. Polyethylene (3.0 g; M_n = 20,000; $Đ$ = 4.8) and a catalyst (5.5 mg) were placed into the glass-lined reaction vessel. The reactor was assembled and the system was evacuated under reduced pressure (100 Pa) and then refilled with Ar (3×). H_2 was introduced to the desired pressure (0.482 MPa) at room temperature and the reactor was sealed. The reactor was heated to 300 °C and the gauge pressure was increased to 0.896 MPa for experiments running for 2–20 h. All pressure values are reported as the absolute pressure at the reaction temperature (0.992 MPa = 0.896 MPa on the pressure gauge). At the end of the designated time, the reactor was allowed to cool to room temperature. The volatile products were sampled by connecting the cooled reactor to a gas chromatography sampling loop and analysed using a gas chromatography flame ionized detector (FID) and gas chromatography thermal conductivity detector. The mass yield of gas-phase products was obtained from direct gas chromatography-calibrated quantitative analysis of C_1–C_9 hydrocarbons separated on an Agilent Technologies 5890 gas chromatograph using an Agilent J&W GS-GasPro (0.32 mm × 15 m) capillary column (gas chromatography FID). H_2 was quantified with respect to a He internal standard using a Supelco Carboxen 1000 (4.6 m × 3.175 mm × 2.1 mm stainless steel) packed column (gas chromatography thermal conductivity detector). Dichloromethane was added to the reactor, which was resealed and heated to 100 °C. The reactor was cooled and the mixture was filtered on a Büchner funnel to separate residual insoluble polymer from the dichloromethane-soluble liquid products. The volatile components were evaporated in a rotary evaporator and the yields of extracted liquid species and solid materials were measured. The soluble materials were analysed by calibrated gas chromatography mass spectrometry using an Agilent Technologies 7890A GC system equipped with a FID or an Agilent Technologies 5975C inert MSD mass spectrometer on an Agilent J&W DB-5ht ((5%-phenyl)-methylpolysiloxane; 0.25 mm × 30 m × 0.1 µm) capillary column (see the section 'Quantification of liquid products' for details). The solid portion was dissolved in 1,2,4-trichlorobenzene (TCB) at 150 °C and analysed by high-temperature gel permeation chromatography (HT-GPC).

Analysis of the reaction products

The solid polymeric residue was analysed by HT-GPC (Agilent-Polymer Laboratories 220) to determine the molecular weights (M_n and M_w) and molecular weight distributions ($Đ = M_w/M_n$). The HT-GPC was equipped with refractive index and viscometry detectors. Monodisperse polyethylene standards (PSS Polymer Standards Service) were used for calibration ranging from ~330 Da to ~120 kDa. The column set included three Agilent PLgel MIXED-B columns and one PLgel Mixed-B Guard column. TCB containing 0.01 wt% 3,5-di-*tert*-butyl-4-hydroxytoluene was used as the eluent at a flow rate of 1.0 ml min^{-1} at 160 °C. The lubricant samples were prepared in TCB at a concentration of ~5.0 mg ml^{-1} and heated at 150 °C for 24 h before injection.

Quantification of liquid products

The composition of the dichloromethane-extracted liquid products, in terms of amounts of each chain length in the samples, was estimated

using our previously reported approach[16], summarized here briefly for convenience. Gas chromatography mass spectrometry of the ASTM standard was integrated. A plot of the integrated area versus the carbon number allowed determination of the response of all C_n values (since the ASTM standard does not include C_{13}, C_{19}, C_{21} and so on) by interpolation. The regions of C_6–C_{20} and C_{20}–C_{40} are linear, but with inequivalent slopes. Therefore, these two regions were fit separately and used as calibration curves for liquid products.

Estimation of C–C bond cleavage from mass balance

M_n can be calculated as the total weight of polymer W divided by the total number of chains N. Under reaction, the number of chains grows over time, with each cleavage reaction producing one new chain. The number of chains may then be expressed as

$$N(t) = N(0) + \int_0^t r_{cut} dt \quad (1)$$

where r_{cut} is the rate of cleavage in cuts per unit time. This may be substituted into the expression for M_n:

$$M_n(t) = \frac{W}{N(t)} = \frac{M_n(0)W}{W + M_n(0)\int_0^t r_{cut} dt} \quad (2)$$

Assuming the cleavage rate is constant and rearranging for r_{cut}:

$$r_{cut} = \frac{W}{t}\left(\frac{1}{M_n(t)} - \frac{1}{M_n(0)}\right) \quad (3)$$

For this relationship to be accurate, the M_n used must be that of the entire population. As the polymer in this work was analysed in separate groups depending on the molecular weight, these analyses must be combined to determine the overall M_n. As the number average is the first moment of the distribution, the M_n of the entire population is the weighted average of the groups:

$$M_{n,total} = \frac{\sum W_i M_{n,i}}{\sum W_i} \quad (4)$$

where the W_i is the mass of an analysed group, $M_{n,i}$ is its number-averaged molecular weight and the summations are over all analysed groups. This result is valid for any number of groups and is true even when polymers of the same size may exist in multiple groups. $M_{n,total}$ may then be used to estimate the C–C bond cleavage rate, per equation (3).

DFT calculations

DFT calculations related to the reaction network of hexane activation over the ZrO_xH_y models supported on the (−111) surface of monoclinic ZrO_2 were performed using the periodic plane-wave code Vienna ab initio simulation package (VASP 5.4)[43,44]. The ion–electron interaction was described by pseudopotentials constructed within the projector augmented wave framework[45]. The Perdew–Burke–Ernzerhof[46] functional form of the generalized gradient approximation was used to treat electron exchange–correlation effects and Grimme's DFT-D3[47] method was used to semiempirically describe the van der Waals interactions. To partially account for the self-interaction errors associated with the generalized gradient approximation Perdew–Burke–Ernzerhof functional, we used the DFT+U methodology by setting the U–J value for the 4d states of Zr to 4 eV[22]. For the structure relaxation, we sampled the Brillouin zone by a 2 × 2 × 1 Monkhorst–Pack k-mesh applying a Gaussian smearing approach (σ = 0.05 eV) with a plane-wave kinetic energy cut-off of 500 eV. All of the calculations included dipole and quadrupole corrections for the energies as implemented in VASP using a modified version of the Makov and Payne method[48], and Harris–Foulke-type corrections[49] were applied for the forces. The transition state structures were determined using the climbing image nudged elastic band[50] and dimer methods[51].

Microkinetic CSTR model for hexane hydrogenolysis over the ZrO_xH_y/m-ZrO_2 model

The rate constants for elementary surface reactions and adsorption processes were calculated using classical harmonic transition state theory and collision theory, respectively. A detailed description of the methodology can be found in our recent report[52]. Vibrational frequencies (ν_i) obtained from DFT calculations were used to calculate the zero-point energy and vibrational partition functions of the intermediate and transition states. Small computed vibrational frequencies (<50 cm^{-1}) for surface species were shifted to 50 cm^{-1} since the harmonic approximation cannot accurately predict these small frequencies (these frequencies in effect cancel out). The number of active sites per surface area used to calculate adsorption rate constants was 2.5×10^{19} m^{-2}. The entropy term for hexane adsorption was calculated using the empirical formula $S_{ad}^0(T) = 0.70 \times S_{gas}^0(T) - 3.3R$, derived by Campbell and Sellers[53].

The CSTR model was constructed under the assumption of an isobaric and isothermal reactor. The species balance for the ideal gas-phase reactants and products was described as:

$$\frac{\partial y_{i,gas}}{\partial\left(\frac{t}{\tau}\right)} = y_{i,gas,0} - y_{i,gas}\left(1 + \tau \times \alpha \sum_i r_{i,gas}\right) + \tau \times \alpha \times r_{i,gas} \quad (5)$$

where $y_{i,gas,0}$ and $y_{i,gas}$ correspond to the inlet and outlet mole fractions of gas species i, respectively, t is the time, τ represents a residence time defined as the ratio of the total mole number of gas molecules in the reactor over the total feed flow rate at reactor entrance conditions $\tau = N_{tot,0}/F_{tot,0}$, α is the total number of active sites in the reactor over the total mole number of gas molecules in the reactor $N_{cat}/N_{tot,0}$ and $r_{i,gas}$ designates a generation rate of gas species i per active site. With the assumption of a constant surface density for the catalyst under various reaction conditions, the value of α was fixed at 1×10^{-3} and $y_{i,gas}$ was calculated by varying τ at a fixed temperature. The steady-state reactor outlet composition, $y_{i,gas}$, and overall conversion only depend on the product of $\alpha \times \tau = N_{cat}/F_{tot,0}$. Thus, meaningful values of $\alpha \times \tau$ can be obtained from the conversion, and predicting the reactor outlet composition for different τ values is equivalent to predicting the outlet composition for different conversion levels.

PHIP study

Hydrogenation of propene over L-ZrO_2@mSiO_2 was examined by adiabatic longitudinal transport after dissociation engenders net alignment (ALTADENA)[41] NMR experiments using 99% enriched pH_2. The pH_2 gas was produced by flowing H_2 (Airgas; UHP) through a cryocooled pH_2 converter (Advanced Research Systems) with a catalyst compartment packed with 46 g FeO(OH) (Sigma–Aldrich) at 20 K. The pH_2 and propene (Airgas; UHP) were mixed by combining the outlets of the mass flow controllers (Alicat) for each gas with a total flow rate of 60 sccm and a pH_2:propene ratio of 5:1. Experiments were performed using 64.9 mg L-ZrO_2@mSiO_2 packed into a 304 stainless steel reactor tube (McMaster-Carr; 5 cm length; 6.35 mm outer diameter; 3.86 mm internal diameter). The catalyst material was held in place using quartz wool and porous 316 L stainless steel frits (McMaster-Carr; 10 µm pore size) on both ends of the reactor tube. The reactor was mounted in the 4.5 mT fringe field of the 9.4 T Bruker Avance wide bore magnet. The catalyst was pre-treated by flowing an H_2/N_2 mixture (total flow rate = 50 ml min^{-1}; 10% H_2) through the reactor at 550 °C for 6 h. Propene hydrogenation was carried out by flowing the pH_2/propene mixture through the catalyst bed at 300 °C at an inlet pressure of 0.294 MPa. The reactor effluent was then transported to the detection coil of a Varian 400 MHz triple-resonance IFC-flow NMR probe at high field

Table 2 | Hydrogenation of propene over L-ZrO_2@mSiO_2—ALTADENA-PHIP NMR results

Conversion	Signal enhancement	Pairwise selectivity (assuming 99% pH_2)	Corrected pairwise selectivity	Observed pH_2 enrichment
5.42±0.55%	78.5±11.4	0.255±0.036%	0.558±0.079%	58.7%

(9.4 T) via flow of the gas through approximately 110 cm of 1.59 mm outer diameter PEEK tubing (0.51 mm internal diameter). The ^{1}H NMR spectrum of the reactor effluent was collected on a 400 MHz Varian VNMRS spectrometer. The continuous-flow hyperpolarized spectrum was acquired by signal averaging of 32 transients using a recycle delay of 1 s and an acquisition time of 0.2 s. The thermally polarized spectrum was acquired after sealing the gas in the NMR probe and signal averaging of 32 transients using a recycle delay of 5 s and an acquisition time of 0.5 s. The propene hydrogenation with normal (n)H_2 (a thermal equilibrium 3:1 mixture of ortho and pH_2) was also performed under identical conditions. The pure ALTADENA spectrum was obtained by subtracting the continous-flow NMR spectrum acquired using nH_2 from the spectrum acquired with 99% pH_2. To ensure that the ALTADENA signal was due to hydrogenation over the L-ZrO_2@mSiO_2 catalyst and not from any other contaminant or metal in the reactor system, control experiments were performed using 99% pH_2 and a reactor tube packed only with an inert filler material (quartz wool). The experimental conditions were otherwise identical. The empty reactor did not yield any detectable conversion, but it did produce a small propane ALTADENA signal with an intensity of ~5% relative to the signal acquired using the L-ZrO_2@mSiO_2 catalyst at 300 °C. The small background NMR signal appeared to arise from the stainless steel surfaces in the reactor and had been observed in our laboratory previously.

Calculation of conversion

The fractional conversion of propene to propane (PA) was calculated from the thermally polarized (TP) spectrum using the following equations:

$$S^{TP}_{PA,^1H} = \frac{S^{TP}_{PA,CH_3}/6 - X_{imp} \times S^{TP}_{Propene,CH}}{1 + X_{imp}} \quad (6)$$

$$\chi = \left(\frac{S^{TP}_{PA,^1H}}{S^{TP}_{PA,^1H} + S^{TP}_{Propene,CH}} \right) \times 100\% \quad (7)$$

where χ is the conversion of propene to propane, S^{TP}_{PA,CH_3} is the measured integral of the PA CH_3 peak in the thermally polarized spectrum, $S^{TP}_{Propene,CH}$ is the measured integral of the propene CH peak in the thermally polarized spectrum, $S^{TP}_{PA,^1H}$ is the calculated integral per proton of PA after the correction of PA impurity and X_{imp} is the percentage impurity of PA in stock propene (0.26%).

Calculation of signal enhancement

The experimental ALTADENA NMR signal enhancement (ε) was evaluated by subtracting the ALTADENA integral of PA CH_3 for the experiment using a stainless steel cartridge with inert fillers from that using L-ZrO_2@mSiO_2, then comparing it with the PA CH_3 peak integral of the thermally polarized spectrum:

$$\varepsilon = \frac{S^{ZrO_2}_{PA,CH_3} - S^{SS}_{PA,CH_3}}{S^{TP}_{PA,^1H}} \quad (8)$$

where $S^{ZrO_2}_{PA,CH_3}$ is the integral of the PA CH_3 peak in the ALTADENA spectrum of experiments catalysed by L-ZrO_2@mSiO_2 and S^{SS}_{PA,CH_3} is the integral of the PA CH_3 peak in the ALTADENA spectrum of experiments catalysed by the stainless steel cartridge with inert fillers.

Calculation of pairwise selectivity

The pairwise selectivity (φ) was obtained by dividing the experimental ALTADENA NMR signal enhancement (ε) by the theoretical value (ε^{theor}, assuming 100% pairwise addition), as in equation (9).

$$\varphi = \frac{\varepsilon}{\varepsilon^{theor}} \times 100\% \quad (9)$$

For the CH_3 proton of PA, the theoretical ALTADENA signal enhancement was obtained from equation (10)[54,55].

$$\varepsilon^{theor}_{ALTADENA} = \frac{2k_B T(4\chi_p - 1)}{3\hbar\gamma_H B_0} \quad (10)$$

where T is the temperature, γ_H is the ^{1}H gyromagnetic ratio (in rad s^{-1}), B_0 is the static magnetic field and χ_p is the para-enrichment. When T = 300 K, B_0 = 9.4 T and χ_p = 99%, $\varepsilon^{theor}_{ALTADENA}$ = 31,524.

Due to the back-conversion of pH_2 to nH_2 by the catalyst during propene hydrogenation, the actual para-enrichment of the H_2 gas within the reactor could be lower than 99%. Indeed, the para-enrichment observed under reaction conditions was only χ'_p = 58.7% (Table 2), as estimated from equation (11):

$$\chi'_p = \left(1 - \frac{3S_{pH_2}}{4S_{nH_2}}\right) \times 100\% \quad (11)$$

where S_{pH_2} and S_{nH_2} represent the integrals of the nH_2 peak in spectra acquired with pH_2 and nH_2, respectively, in the presence of propene, under reaction conditions. The corrected pairwise selectivity (φ') was then obtained using equations (9)–(11).

Data availability

The authors declare that the data supporting the findings of this study are available within the paper and its Supplementary Information files or from the corresponding authors upon reasonable request. Atomic coordinates from calculations, NMR spectra and chromatography data that support the findings of this study are available in DataShare at https://doi.org/10.25380/iastate.21725192. Source data are provided with this paper.

References

1. Lwin, S. & Wachs, I. E. Olefin metathesis by supported metal oxide catalysts. *ACS Catal.* **4**, 2505–2520 (2014).
2. Sinfelt, J. H., Taylor, W. F. & Yates, D. J. C. Catalysis over supported metals. III. Comparison of metals of known surface area for ethane hydrogenolysis. *J. Phys. Chem.* **69**, 95–101 (1965).
3. Gillespie, W. D., Herz, R. K., Petersen, E. E. & Somorjai, G. A. The structure sensitivity of *n*-heptane dehydrocyclization and hydrogenolysis catalyzed by platinum single crystals at atmospheric pressure. *J. Catal.* **70**, 147–159 (1981).
4. Flaherty, D. W. & Iglesia, E. Transition-state enthalpy and entropy effects on reactivity and selectivity in hydrogenolysis of *n*-alkanes. *J. Am. Chem. Soc.* **135**, 18586–18599 (2013).
5. Weitkamp, J. Catalytic hydrocracking—mechanisms and versatility of the process. *ChemCatChem* **4**, 292–306 (2012).
6. Geyer, R., Jambeck, J. R. & Law, K. L. Production, use, and fate of all plastics ever made. *Sci. Adv.* **3**, e1700782 (2017).

7. De Smet, M. *The New Plastics Economy: Rethinking the Future of Plastics*. Report No. 080116 (Ellen Macarthur Foundation, 2016).
8. Celik, G. et al. Upcycling single-use polyethylene into high-quality liquid products. *ACS Cent. Sci.* **5**, 1795–1803 (2019).
9. Liu, S., Kots, P. A., Vance, B. C., Danielson, A. & Vlachos, D. G. Plastic waste to fuels by hydrocracking at mild conditions. *Sci. Adv.* **7**, eabf8283 (2021).
10. Rorrer, J. E., Beckham, G. T. & Román-Leshkov, Y. Conversion of polyolefin waste to liquid alkanes with Ru-based catalysts under mild conditions. *JACS Au* **1**, 8–12 (2021).
11. Nakaji, Y. et al. Low-temperature catalytic upgrading of waste polyolefinic plastics into liquid fuels and waxes. *Appl. Catal. B* **285**, 119805 (2021).
12. Jaydev, S. D., Martín, A. J. & Pérez-Ramírez, J. Direct conversion of polypropylene into liquid hydrocarbons on carbon-supported platinum catalysts. *ChemSusChem* **14**, 5179–5185 (2021).
13. O'Reilly, M. E., Dutta, S. & Veige, A. S. β-Alkyl elimination: fundamental principles and some applications. *Chem. Rev.* **116**, 8105–8145 (2016).
14. Kanbur, U. et al. Catalytic carbon–carbon bond cleavage and carbon–element bond formation give new life for polyolefins as biodegradable surfactants. *Chem* **7**, 1347–1362 (2021).
15. Dufaud, V. & Basset, J.-M. Catalytic hydrogenolysis at low temperature and pressure of polyethylene and polypropylene to diesels or lower alkanes by a zirconium hydride supported on silica-alumina: a step toward polyolefin degradation by the microscopic reverse of Ziegler–Natta polymerization. *Angew. Chem. Int. Ed.* **37**, 806–810 (1998).
16. Tennakoon, A. et al. Catalytic upcycling of high-density polyethylene via a processive mechanism. *Nat. Catal.* **3**, 893–901 (2020).
17. Wu, X. et al. Size-controlled nanoparticles embedded in a mesoporous architecture leading to efficient and selective hydrogenolysis of polyolefins. *J. Am. Chem. Soc.* **144**, 5323–5334 (2022).
18. Kobayashi, T., Singappuli-Arachchige, D., Wang, Z., Slowing, I. I. & Pruski, M. Spatial distribution of organic functional groups supported on mesoporous silica nanoparticles: a study by conventional and DNP-enhanced ^{29}Si solid-state NMR. *Phys. Chem. Chem. Phys.* **19**, 1781–1789 (2017).
19. Kondo, J., Domen, K., Maruya, K.-I. & Onishi, T. Infrared studies of ethene hydrogenation over ZrO_2. Part 3.—Reaction mechanism. *J. Chem. Soc. Faraday Trans.* **88**, 2095–2099 (1992).
20. Hoang, D. L. & Lieske, H. Effect of hydrogen treatments on ZrO_2 and Pt/ZrO_2 catalysts. *Catal. Lett.* **27**, 33–42 (1994).
21. Utami, M. et al. Hydrothermal preparation of a platinum-loaded sulphated nanozirconia catalyst for the effective conversion of waste low density polyethylene into gasoline-range hydrocarbons. *RSC Adv.* **9**, 41392–41401 (2019).
22. Puigdollers, A. R., Tosoni, S. & Pacchioni, G. Turning a nonreducible into a reducible oxide via nanostructuring: opposite behavior of bulk ZrO_2 and ZrO_2 nanoparticles toward H_2 adsorption. *J. Phys. Chem. C* **120**, 15329–15337 (2016).
23. Zhang, Y. et al. Control of coordinatively unsaturated Zr sites in ZrO_2 for efficient C–H bond activation. *Nat. Commun.* **9**, 3794 (2018).
24. Arce-Ramos, J.-M., Grabow, L. C., Handy, B. E. & Cárdenas-Galindo, M.-G. Nature of acid sites in silica-supported zirconium oxide: a combined experimental and periodic DFT study. *J. Phys. Chem. C* **119**, 15150–15159 (2015).
25. Yang, S. et al. Graphene-based nanosheets with a sandwich. *Struct. Angew. Chem. Int. Ed.* **49**, 4795–4799 (2010).
26. Wang, Z.-M., Wang, W., Coombs, N., Soheilnia, N. & Ozin, G. A. Graphene oxide–periodic mesoporous silica sandwich nanocomposites with vertically oriented channels. *ACS Nano* **4**, 7437–7450 (2010).
27. Wang, Z.-M. et al. Sandwich-type nanocomposite of reduced graphene oxide and periodic mesoporous silica with vertically aligned mesochannels of tunable pore depth and size. *Adv. Func. Mater.* **27**, 1704066 (2017).
28. Lesage, A. et al. Surface enhanced NMR spectroscopy by dynamic nuclear polarization. *J. Am. Chem. Soc.* **132**, 15459–15461 (2010).
29. Shen, L. et al. ^{17}O solid-state NMR studies of ZrO_2 nanoparticles. *J. Phys. Chem. C* **123**, 4158–4167 (2019).
30. Perras, F. A., Kobayashi, T. & Pruski, M. Natural abundance ^{17}O DNP two-dimensional and surface-enhanced NMR spectroscopy. *J. Am. Chem. Soc.* **137**, 8336–8339 (2015).
31. Perras, F. A., Boteju, K. C., Slowing, I. I., Sadow, A. D. & Pruski, M. Direct ^{17}O dynamic nuclear polarization of single-site heterogeneous catalysts. *Chem. Commun.* **54**, 3472–3475 (2018).
32. Petkov, V., Holzhüter, G., Tröge, U., Gerber, T. & Himmel, B. Atomic-scale structure of amorphous TiO_2 by electron, X-ray diffraction and reverse Monte Carlo simulations. *J. Non. Cryst. Solids* **231**, 17–30 (1998).
33. Lee, S. K., Lee, S. B., Park, S. Y., Yi, Y. S. & Ahn, C. W. Structure of amorphous aluminum oxide. *Phys. Rev. Lett.* **103**, 095501 (2009).
34. Buchholz, D. B. et al. The structure and properties of amorphous indium oxide. *Chem. Mater.* **26**, 5401–5411 (2014).
35. Strand, J. et al. Intrinsic charge trapping in amorphous oxide films: status and challenges. *J. Phys. Condens. Matter* **30**, 233001 (2018).
36. Onishi, T., Abe, H., Maruya, K.-I. & Domen, K. IR spectra of hydrogen adsorbed on ZrO_2. *J. Chem. Soc. Chem. Commun.* **1985**, 617–618 (1985).
37. Hicks, K. E. et al. Zr_6O_8 node-catalyzed butene hydrogenation and isomerization in the metal–organic framework NU-1000. *ACS Catal.* **10**, 14959–14970 (2020).
38. Walsh, P. J., Hollander, F. J. & Bergman, R. G. Generation, alkyne cycloaddition, arene carbon–hydrogen activation, nitrogen–hydrogen activation and dative ligand trapping reactions of the first monomeric imidozirconocene (Cp_2Zr:NR) complexes. *J. Am. Chem. Soc.* **110**, 8729–8731 (1988).
39. Cummins, C. C., Baxter, S. M. & Wolczanski, P. T. Methane and benzene activation via transient (*tert*-$Bu_3SiNH)_2Zr$=NSi-*tert*-Bu_3. *J. Am. Chem. Soc.* **110**, 8731–8733 (1988).
40. Corker, J. et al. Catalytic cleavage of the C–H and C–C bonds of alkanes by surface organometallic chemistry: an EXAFS and IR characterization of a Zr–H catalyst. *Science* **271**, 966–969 (1996).
41. Pravica, M. G. & Weitekamp, D. P. Net NMR alignment by adiabatic transport of parahydrogen addition products to high magnetic field. *Chem. Phys. Lett.* **145**, 255–258 (1988).
42. Bowers, C. R. & Weitekamp, D. P. Parahydrogen and synthesis allow dramatically enhanced nuclear alignment. *J. Am. Chem. Soc.* **109**, 5541–5542 (1987).
43. Kresse, G. & Hafner, J. Ab initio molecular-dynamics simulation of the liquid-metal–amorphous-semiconductor transition in germanium. *Phys. Rev. B* **49**, 14251–14269 (1994).
44. Kresse, G. & Furthmüller, J. Efficiency of ab-initio total energy calculations for metals and semiconductors using a plane-wave basis set. *Comput. Mater. Sci.* **6**, 15–50 (1996).
45. Blöchl, P. E. Projector augmented-wave method. *Phys. Rev. B* **50**, 17953–17979 (1994).
46. Perdew, J. P., Burke, K. & Ernzerhof, M. Generalized gradient approximation made simple. *Phys. Rev. Lett.* **77**, 3865–3868 (1996).

47. Grimme, S., Antony, J., Ehrlich, S. & Krieg, H. A consistent and accurate ab initio parametrization of density functional dispersion correction (DFT-D) for the 94 elements H–Pu. *J. Chem. Phys.* **132**, 154104 (2010).
48. Makov, G. & Payne, M. C. Periodic boundary conditions in ab initio calculations. *Phys. Rev. B* **51**, 4014–4022 (1995).
49. Harris, J. Simplified method for calculating the energy of weakly interacting fragments. *Phys. Rev. B* **31**, 1770–1779 (1985).
50. Henkelman, G., Uberuaga, B. P. & Jónsson, H. A climbing image nudged elastic band method for finding saddle points and minimum energy paths. *J. Chem. Phys.* **113**, 9901–9904 (2000).
51. Heyden, A., Bell, A. T. & Keil, F. J. Efficient methods for finding transition states in chemical reactions: comparison of improved dimer method and partitioned rational function optimization method. *J. Chem. Phys.* **123**, 224101 (2005).
52. You, K.-E., Ammal, S. C., Lin, Z. & Heyden, A. Understanding selective hydrodeoxygenation of 1,2- and 1,3-propanediols on Cu/Mo_2C via multiscale modeling. *ACS Catal.* **12**, 4581–4596 (2022).
53. Campbell, C. T. & Sellers, J. R. V. The entropies of adsorbed molecules. *J. Am. Chem. Soc.* **134**, 18109–18115 (2012).
54. Zhao, E. W. et al. Silica-encapsulated Pt–Sn intermetallic nanoparticles: a robust catalytic platform for parahydrogen-induced polarization of gases and liquids. *Angew. Chem. Int. Ed.* **56**, 3925–3929 (2017).
55. Bowers, C. R. Sensitivity enhancement utilizing parahydrogen. *eMagRes* https://doi.org/10.1002/9780470034590.emrstm0489 (2007).

Acknowledgements

This work was supported by the Institute for Cooperative Upcycling of Plastics (iCOUP), an Energy Frontier Research Center funded by the US Department of Energy (DOE) Office of Basic Energy Sciences. The Ames Laboratory is operated by Iowa State University under contract DE-AC-02-07CH11358 (S.C., A.T., K.-E.Y., A.L.P., R.Y., M.S., B.P., K.R.P., S.C.A., F.A.P., A.H., A.D.S. and W.H.) and the Argonne National Laboratory is operated by the UChicago Argonne under contract DE-AC-02-06CH11357 (L.F., R.A.H., M.D., T.L. and B.L.). S.C.A. and A.H. acknowledge partial support from the South Carolina Smart State Center for Strategic Approaches to the Generation of Electricity (SAGE). The pH_2 labelling experiments were supported by National Science Foundation grant CHE-2108306 (T.Y.Z., M.P.L. and C.R.B.) and the National High Magnetic Field Laboratory is supported by the National Science Foundation through NSF/DMR-2128556* and the state of Florida.. This research used resources of the Advanced Photon Source, a DOE Office of Science User Facility operated for the DOE Office of Science by Argonne National Laboratory under contract AC02-06CH11357 (L.F., T.L. and B.L.). Computational resources were provided by XSEDE Resources, located at the San Diego Supercomputer Center, and Texas Advanced Computing Center grant TG-CTS090100 (K.-E.Y., S.C.A. and A.H.), as well as the National Energy Research Scientific Computing Center (NERSC) under contract DE-AC02-05CH11231 (K.-E.Y., S.C.A. and A.H.).

Author contributions

S.C. prepared and characterized the zirconia catalysts under the direction of W.H. The catalytic experiments were performed by A.T. and M.S guided by A.D.S. The analysis of liquid products was performed by A.T., M.S., Y.-Y.W., X.W. and L.Q., guided by A.D.S. and W.H. GPC was performed by R.A.H. under the supervision of M.D. Theoretical calculations were performed by K.-E.Y. and S.C.A., directed by A.H. The numbers of C–C bond cleavage steps were calculated by R.Y. using the model created by B.P. Characterization by solid-state nuclear magnetic resonance was conducted by A.L.P. under the direction of F.A.P. Characterization by X-ray absorption spectroscopy was conducted by L.F., T.L. and B.L. Characterization by ICP-MS was conducted by S.C. and X.W. The DRIFT experiments were performed by S.A. and K.R.P. The PHIP experiments were performed by T.Y.Z., M.P.L, and C.R.B. The manuscript was composed by S.C., A.T., K.-E.Y., A.H., W.H., and A.D.S. with contributions from all other co-authors.

Competing interests

The authors declare no competing interests.

Additional information

Supplementary information The online version contains supplementary material available at https://doi.org/10.1038/s41929-023-00910-x.

Correspondence and requests for materials should be addressed to Andreas Heyden, Aaron D. Sadow or Wenyu Huang.

Peer review information *Nature Catalysis* thanks Bert Weckhuysen, Kinga Gora-Marek and the other, anonymous, reviewer(s) for their contribution to the peer review of this work.